Research Square

Preprints are preliminary reports that have not undergone peer review.
They should not be considered conclusive, used to inform clinical practice,
or referenced by the media as validated information.

Reliable Underground-to-Aboveground Communications with Magnetic Transmitters and Electric Receivers

Guozheng Zhao
Huazhong University of Science and Technology
Guanghua Liu
guanghualiu@hust.edu.cn
Huazhong University of Science and Technology
Yi Liu
Huazhong University of Science and Technology
Xiran Guo
Huazhong University of Science and Technology
Zhangyu Li
South Central Minzu University

Article

Keywords:

Posted Date: November 2nd, 2026

DOI: https://doi.org/10.21203/rs.3.rs-11173601/v1

License: This work is licensed under a Creative Commons Attribution 4.0 International License.
Read Full License

Additional Declarations: No competing interests reported.

Reliable Underground-to-Aboveground Communications with Magnetic Transmitters and Electric Receivers

Guozheng Zhao[1], Guanghua Liu[1*], Yi Liu[1], Xiran Guo[1], Zhangyu Li[2]

[1]School of Cyber Science and Engineering, Huazhong University of Science and Technology, Luoyu Road, Wuhan, 430074, Hubei, China.
[2]College of Electronics and Information Engineering (School of Robotics), South-Central Minzu University, Minzu Avenue, Wuhan, 430074, Hubei, China.

*Corresponding author(s). E-mail(s): guanghualiu@hust.edu.cn;
Contributing authors: guozheng_zhao@hust.edu.cn;
yiliu6868@hust.edu.cn; guoxiran@hust.edu.cn; zhangyuli@scuec.edu.cn;

Abstract

Unlike conventional electric- or magnetic-antenna transceiver systems, the magnetic transmitters and electric receivers (MTER) system jointly exploits the induction and radiation fields, providing a new solution to enable both deep underground transmission and long-range aboveground communication. However, the maximum reliable aboveground coverage achievable by MTER-enabled UG2AG communications has not yet been systematically studied, which is essential for guiding transmitter configuration and practical gateway deployment. In this paper, we develop a reliability-oriented framework to maximize the aboveground coverage of MTER-enabled UG2AG communication through transmitter configuration and operating-frequency design. Specifically, we first establish a reliable-coverage model that links the MTER link characteristics to the achievable aboveground communication range. Furthermore, we determine the transmitter configuration and operating frequency to maximize the reliable coverage under practical system constraints. Finally, we evaluate the proposed solution under different underground environments and validate the MTER link through a field experiment in an underground mine. The results show that transmitter configuration optimization can effectively extend the reliable aboveground coverage, and the optimal transmitter configuration is environment-dependent.

In addition, the MTER link can support successful end-to-end data transmission in a realistic underground environment.

Keywords: Magnetic transmitters and electric receivers, underground to aboveground communication, reliable coverage, transmitter configuration.

Main

Wireless underground-to-aboveground (UG2AG) communications play an important role in certain applications, such as underground infrastructure monitoring, underground environment sensing, mine safety, and the underground Internet of Things [1–4]. In conventional UG2AG communications, electromagnetic (EM) wave communications based on electric antennas are adopted to transmit data [5–8]. For example, UG2AG communication based on electric antennas using Long Range (LoRa) has been extensively investigated for underground monitoring because of its capability for long-range aboveground connectivity [9–12]. However, its underground performance is fundamentally constrained by the strong absorption and attenuation of EM waves in lossy soil, which severely limits the communication depth [13].

To improve the underground transmission distance, some studies use magnetic induction (MI) communications based on magnetic antennas to address the strong signal attenuation of EM wave techniques [14–17]. This is because the underground medium hardly changes the attenuation rate of magnetic fields [18]. By utilizing the MI communication technology, the underground transmission range can exceed 6 m [19]. However, the communication range of MI is fundamentally limited by the spatial extent of the induction field, making it difficult to support long-range aboveground connectivity in UG2AG scenarios.

To overcome this limitation, Zhao et al. [20] first propose the magnetic-transmitter-to-electric-receiver (MTER) system for UG2AG communication by jointly exploiting the induction and radiation fields and demonstrate its feasibility for deep underground and long-range aboveground communication through channel modeling and performance evaluation. In this architecture, underground magnetic transmitters enable signals to propagate through areas dominated by induction, with relatively low underground attenuation. Furthermore, radiated components subsequently facilitate long-distance propagation towards the surface. In this way, MTER combines the underground penetration advantages of magnetic transmission with the long-range coverage capabilities of radiated communication, offering a promising approach for simultaneously supporting deep underground communication and extended surface connectivity.

Despite this potential, translating the propagation advantage of MTER into reliable and deployable UG2AG connectivity remains an open issue. In many underground sensing and monitoring applications, the location and burial depth of equipment are mainly determined by the monitoring object, geological conditions, or the sensing task itself, making it difficult to freely adjust the position of underground nodes in

order to improve communication performance [21]. In contrast, ground gateways typically have higher deployment flexibility. Therefore, after the underground nodes have been installed, the real issue that the communication system needs to focus on is not just how to reduce path loss, but how to expand the surface area that can stably receive its information while meeting the given reliability requirements [22]. A larger reliable coverage area on the ground can reduce the deployment density of ground gateways, improve the flexibility of gateway location selection, and directly improve the deployability of the system.

To improve the reliable coverage of the MTER-enabled UG2AG system, an effective method is to jointly configure the underground transmitting antenna and the operating frequency. This is because the loop radius and number of turns affect the ohmic loss, radiation resistance, inductive characteristics, radiation efficiency, and available bandwidth of the transmitter [23–25], thereby determining both how efficiently the input power can be converted into radiated energy and whether the required communication bandwidth can be supported. Meanwhile, lower frequencies generally favour underground penetration and extend the induction-dominated region, but reduce the radiation capability of an electrically small loop, whereas higher frequencies can enhance radiation while increasing underground attenuation and shortening the induction-dominated region [26–28]. Therefore, the transmitter configuration and operating frequency jointly determine the balance among radiation capability, underground propagation loss, and bandwidth feasibility, and ultimately determine the achievable reliable aboveground coverage.

Existing studies on MTER have focused on characterizing its propagation behaviour and evaluating communication performance under predetermined transmitter configurations. The effects of underground environments and antenna parameters on path loss, channel capacity, and bit-error performance have been investigated, demonstrating the feasibility of MTER for deep UG2AG communication. However, these analyses mainly reveal how individual parameters affect link performance, rather than determining how the transmitter should be configured to maximize reliable aboveground coverage under practical physical and bandwidth constraints. In particular, the coupling among antenna size, number of turns, operating frequency, radiation efficiency, propagation loss, and available bandwidth has not yet been systematically incorporated into a unified coverage-oriented design framework.

In this paper, we investigate reliable aboveground coverage in MTER-enabled UG2AG communications under deep-burial conditions. Specifically, we first develop a reliability-oriented coverage framework for MTER-enabled UG2AG communication. The framework captures the coupled effects of underground propagation, antenna characteristics, and bandwidth requirements. Furthermore, the transmitter configuration and operating frequency are optimized to maximize reliable aboveground coverage under practical constraints. In addition, the resulting design is evaluated across different underground environments. Finally, we implement a USRP-based prototype and conduct a field experiment in an underground mine to examine whether the MTER link can support practical information delivery.

The remainder of this paper is organized as follows. We first introduce the MTER-enabled UG2AG system, establish the reliable coverage model, and present

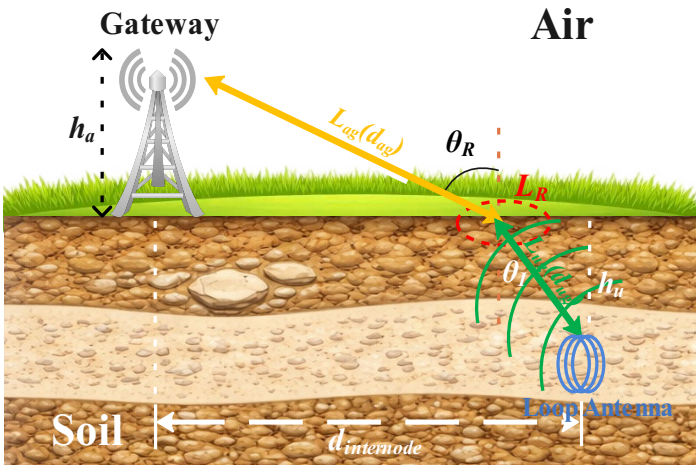


Fig. 1 Architecture of the MTER-enabled UG2AG communication.

the transmitter configuration scheme for improving reliable aboveground coverage in the Methods section. In the Results section, we evaluate the proposed framework under different underground environments and system parameters and present the field experimental results in an underground mine.

Methods

MTER-enabled UG2AG communication system

System model

In this section, we introduce the MTER architecture for UG2AG communication, which is shown in Fig. 1. In this communication architecture, the loop antenna deployed underground and the low- or mid-frequency dipole antenna placed on the gateway aboveground enable large-depth and long-distance UG2AG communication. Specifically, in the underground medium, the small-loop antenna mainly generates an induction-dominated field, whose magnetic component experiences relatively low absorption loss during propagation. Once the signal reaches the aboveground region, the radiation-field component becomes better suited for long-distance transmission and can be efficiently received by an electric antenna. Thus, the MTER architecture combines underground induction-field penetration with aboveground radiation-field coverage, improving the effective UG2AG transmission distance under cross-medium conditions and heterogeneous antenna deployments in practical systems.

In this communication architecture, the underground magnetic transmitter is modeled as a small loop antenna, which is less than 1/4 wavelength ($\lambda/4$) [29]. The burial depth is selected according to the estimated near-field boundary, so that the induction-dominated field can cover the underground segment while the radiating component is mainly formed toward the aboveground region. Under this condition, the path loss model can be explained in two cases based on the relationship between the radiation

boundary and the burial depth of the small loop antenna [20]. On the one hand, when the burial depth of the loop antenna is greater than the radiation boundary, the radiation of EM waves starts from underground and refracts to reach the aboveground. On the other hand, if the burial depth of the loop antenna is less than the radiation boundary, the radiation of EM waves starts from the air. Therefore, the path loss of the MTRE system in UG2AG communications can be expressed as:

When the burial depth of the loop antenna is greater than the radiation boundary,

$$\begin{aligned} \mathrm{PL} &= \frac{1}{\eta\chi^2}\left(\frac{4\pi d_{\mathrm{ug}}}{\lambda_{\mathrm{soil}}}\right)^2 e^{2\alpha d_{\mathrm{ug}}}\frac{(1+\sqrt{\varepsilon'})^2}{4\sqrt{\varepsilon'}}\left(\frac{4\pi d_{\mathrm{ag}}}{\lambda_c}\right)^2 \\ &= \frac{1}{\chi^2}\left(1+\frac{R_{\mathrm{loss}}}{R_{\mathrm{rad,soil}}}\right)\left(\frac{4\pi d_{\mathrm{ug}}}{\lambda_{\mathrm{soil}}}\right)^2 e^{2\alpha d_{\mathrm{ug}}}\times\frac{(1+\sqrt{\varepsilon'})^2}{4\sqrt{\varepsilon'}}\left(\frac{4\pi d_{\mathrm{ag}}}{\lambda_c}\right)^2 \end{aligned} \tag{1}$$

where $d_{ug} = d_{soil} - d_{bdry}$ and $d_{ag} = d_{air}$, where d_{soil} is the burial depth of the antenna, $d_{ag} = d_{air}$ is the transmission distance aboveground, and $d_{bdry} = \lambda/2\pi$ is the boundary where the radiation begins underground. η is the radiation efficiency of the loop antenna in the soil, and χ^2 denotes the slow-varying fading-related power gain. $\lambda_{\mathrm{soil}} = 2\pi/\beta_{soil}$ and λ_{c} are the wavelength in soil and air, respectively. α is the attenuation constant of the soil medium. R_{loss} and $R_{rad,soil}$ are the ohmic loss resistance and the radiation resistance of the transmission antenna in soil, which can be given as:

$$R_{loss} = \frac{Nb}{a}R_s\left(\frac{R_p}{R_0}+1\right) \tag{2}$$

where $R_s = \sqrt{\omega\mu_0/2\sigma}$ is the surface resistivity of a loop antenna, $R_0 = NR_s/2\pi a$ is the resistance per unit length generated by the skin effect, and R_p is the resistance per unit length generated by the proximity effect. The ratio of R_p/R_0 can be computed as a function of the spacing c_{loop}/a [30], which is set to 0.5 in this work. a is the radius of the copper wire, b is the radius of the loop antenna, and c_{loop} is the distance between adjacent loops.

When the burial depth of the loop antenna is less than the radiation boundary,

$$\mathrm{PL} = \frac{1}{\eta\chi^2}\left(\frac{4\pi d_{\mathrm{ag}}}{\lambda_c}\right)^2 = \frac{1}{\chi^2}\left(1+\frac{R_{\mathrm{loss}}}{R_{\mathrm{rad}}}\right)\left(\frac{4\pi d_{\mathrm{ag}}}{\lambda_c}\right)^2 \tag{3}$$

where $d_{ag} = d_{air} - d_{bdry_{air}}$, $d_{bdry_{air}}$ is the part of the induced near-field in the air.

Correspondingly, the radiation resistance can be expressed in two cases. When the burial depth of the loop antenna is greater than the radiation boundary,

$$R_{rad,soil} = \mathrm{Re}\left[\tilde{\eta}_{\mathrm{soil}}\frac{2\pi}{3}\left(\frac{\tilde{k}_{\mathrm{soil}}A_{\mathrm{loop}}}{\lambda_{\mathrm{soil}}}\right)^2 N_t^2\right] \tag{4}$$

where $\widetilde{\eta}_{soil} = \sqrt{\mu/\widetilde{\varepsilon}}$ is the complex wave impedance in the soil, $\widetilde{k}_{soil} = \omega\sqrt{\mu\widetilde{\varepsilon}}$ is the complex wave number in the soil, and A_{loop} is the area of the loop antenna. μ is the conductivity of the soil and $\widetilde{\varepsilon}$ is the complex dielectric constant.

When the burial depth of the loop antenna is less than the radiation boundary,

$$R_{rad} = \eta_{air} \frac{2\pi}{3} \left(\frac{k_{air} A_{\text{loop}}}{\lambda_{air}} \right)^2 \frac{4\sqrt{\varepsilon'_{soil}}}{(\sqrt{\varepsilon'_{soil}} + 1)^2} N^2 \tag{5}$$

In addition, α and β can be calculated by [31]:

$$\alpha = (2\pi c/\lambda_0) \sqrt{(\mu_r \mu_0 \varepsilon' \varepsilon_0/2) \left[\sqrt{1 + (\varepsilon''/\varepsilon')^2} - 1 \right]} \tag{6}$$

$$\beta = (2\pi c/\lambda_0) \sqrt{(\mu_r \mu_0 \varepsilon' \varepsilon_0/2) \left[\sqrt{1 + (\varepsilon''/\varepsilon')^2} + 1 \right]} \tag{7}$$

where ε' and ε'' are the real part and the imaginary part of the soil's dielectric constant, respectively. In the MTER system, the dielectric constant of the soil is calculated by the model from [32] over a frequency range of 10 kHz to 8 GHz.

$$\varepsilon^*_{r,\text{eff}} = \varepsilon'_r - i\varepsilon''_r = \varepsilon^*_{\text{HF}} + \frac{\Delta\varepsilon_{S1}}{1 + i\omega\tau_1} + \frac{\Delta\varepsilon_{S2}}{1 + (i\omega\tau_2)^{1-\alpha_2}} + \frac{\Delta\varepsilon_{S3}}{1 + (i\omega\tau_3)^{1-\alpha_3}} - i\frac{\sigma}{\omega\varepsilon_0} \tag{8}$$

where ε^*_{HF} is the high-frequency limit of the complex dielectric permittivity of the soil. τ_1, τ_2 and τ_3 are relaxation times for them, respectively. $\Delta\varepsilon_{S1}$, $\Delta\varepsilon_{S2}$ and $\Delta\varepsilon_{S3}$ are the strengths of the first, second, and third relaxation processes. α_2 and α_3 are the coefficients of the relaxation time distribution.

In this work, we focus on the deployment regime where the burial depth exceeds the radiation-initiation boundary. In this scenario, the field generated by the small-loop antenna remains predominantly inductive in the near-field region of the underground path. Furthermore, the radiated component begins to form within the soil before reaching the soil–air interface. This operating mechanism is consistent with the deeply buried UG2AG scenario considered in this study and preserves the expected MTER propagation mechanism, which utilises the relatively low underground attenuation of the inductively dominated field, together with radiated field propagation, to enable long-range surface communication.

Transmit-antenna design optimization for reliable coverage

In the MTER-enabled UG2AG communication system, the transmission performance is affected by the transmit-antenna design [20]. Specifically, the antenna radius and turn number jointly determine the radiation efficiency and available bandwidth of the underground transmitter. Furthermore, the operating frequency affects both antenna characteristics and frequency-dependent underground propagation loss. In order to improve the transmission performance, it is essential to jointly optimize the antenna radius, turn number, and operating frequency while accounting for their coupled effects on antenna radiation, bandwidth, and underground propagation.

In this section, reliable aboveground coverage is adopted as the primary performance metric, since it characterizes how far the MTER link can sustain a prescribed

communication reliability under a given transmit-power budget. Based on this, we first establish the reliable-coverage model and formulate the transmitter-configuration optimization problem by jointly considering the antenna radius, turn number, and operating frequency. Moreover, we develop an optimization scheme that accounts for antenna and propagation characteristics to determine the transmitter configuration that maximizes reliable MTER coverage.

Reliable-coverage modeling and problem formulation

According to the above path loss model (Eq.1), we can see that the MTER path loss mainly comprises underground propagation loss, transmission loss across the soil–air interface, and aboveground free-space propagation loss, while also accounting for the transmit-antenna radiation efficiency and the slowly varying channel gain. To explicitly characterize the aboveground coverage, the terms independent of d_{ag} are collected into a compact underground-to-air loss factor $\mathcal{L}_{\mathrm{ug}}(f)$, leaving the aboveground distance dependence explicitly represented by the free-space propagation term. $\mathcal{L}_{\mathrm{ug}}(f)$ can be expressed as:

$$\mathcal{L}_{\mathrm{ug}}(f) = \left(\frac{4\pi d_{\mathrm{ug}}}{\lambda_{\mathrm{soil}}}\right)^2 e^{2\alpha d_{\mathrm{ug}}} \frac{\left(1+\sqrt{\varepsilon'}\right)^2}{4\sqrt{\varepsilon'}} \tag{9}$$

Furthermore, let P_t denote the transmission power and $P_{\mathrm{n}} = k_{\mathrm{B}} T_0 F B_{\mathrm{n}}$ is the receiver-noise power, the received signal-to-noise ratio (SNR) can be shown as:

$$\gamma_{\mathrm{rx}} = \frac{P_{\mathrm{t}} \eta(b, N_{\mathrm{t}}, f) \chi^2 c^2}{16\pi^2 k_{\mathrm{B}} T_0 F B_{\mathrm{n}} f^2 d_{\mathrm{ag}}^2 \mathcal{L}_{\mathrm{ug}}(f)} \tag{10}$$

where k_{B} is the Boltzmann constant, T_0 is the reference noise temperature, F is the receiver noise factor in linear scale, and B_n is the equivalent noise bandwidth determined by the waveform and receiver filtering.

In order to ensure the reliability of link quality, the received SNR γ_{rx} should be no lower than the minimum SNR γ_{req} required to achieve the target packet delivery ratio (PDR) ρ_0. Among these, γ_{req} can be defined as:

$$\gamma_{\mathrm{req}} = \inf\{\gamma : \mathrm{PDR}(\gamma) \geq \rho_0\} \tag{11}$$

Therefore, the maximum reliable aboveground distance $d_{\mathrm{ag,max}}$ can be given as:

$$d_{\mathrm{ag,max}}^2 = \frac{P_{\mathrm{t}} \chi_0^2 c^2}{16\pi^2 \gamma_{\mathrm{req}} k_{\mathrm{B}} T_0 F B_{\mathrm{n}}} \frac{\eta(b, N_{\mathrm{t}}, f)}{f^2 \mathcal{L}_{\mathrm{ug}}(f)} \tag{12}$$

The problem formulation can then be described as:

$$\begin{aligned}
\mathcal{P}_0: \quad & \max_{b,N_t,f} \quad d^2_{\mathrm{ag,max}}(b,N_t,f) \\
& \text{s.t.} \quad b_{\min} \le b \le b_{\max}, \\
& \qquad N_{\min} \le N_t \le N_{\max}, \qquad N_t \in \mathbb{Z}_+, \\
& \qquad f_{\min} \le f \le f_{\max}, \\
& \qquad B_{\mathrm{ant}}(b,N_t,f) \ge B_{\min}, \\
& \qquad \beta(f) b \le \xi_{\mathrm{sl}}, \\
& \qquad \beta(f) d_{\mathrm{soil}} \ge 1.
\end{aligned} \tag{13}$$

where $b_{\min}$ and $b_{\max}$ are the admissible loop-radius limits, $N_{\min}$ and $N_{\max}$ define the allowed integer turn-number range, and $f_{\min}$ and $f_{\max}$ specify the operating-frequency range. The parameter ξ_{sl} specifies the maximum normalized electrical size allowed by the electrically small-loop approximation. The last constraint ensures that the physical burial depth remains beyond the radiation boundary assumed by the propagation model. In addition, the available resonant bandwidth B_{ant} needs to be greater than the minimum required bandwidth $B_{\min}$, in which B_{ant} can be illustrated as:

$$B_{\mathrm{ant}} = \frac{f}{Q_{\mathrm{L}}} = \frac{R_{\mathrm{Q}}}{2\pi L_{\mathrm{c}}} = \frac{R_{\mathrm{loss}} + R_{\mathrm{rad,soil}}}{2\pi L_{\mathrm{c}}} \tag{14}$$

where the inductance of the multi-turn circular loop L_{c} can be approximated by:

$$L_{\mathrm{c}}(b,N_{\mathrm{t}}) = \mu_0 N_{\mathrm{t}}^2 b \left[\ln\left(\frac{8b}{a}\right) - 2\right] \tag{15}$$

Optimization scheme for transmitter configuration

As shown in Eq.13, $\mathcal{P}_0$ contains two continuous variables and one integer variable, while the operating frequency affects the system performance nonlinearly through the dispersive MTER propagation model. A direct joint optimization over (b, N_{t}, f) would not only increase the computational burden, but also obscure the physical relationship between the transmitter configuration and the antenna and propagation characteristics. We therefore exploit the structural dependence of the conductor loss, radiation resistance, and loop inductance on the design variables to reduce the dimensionality of the original problem.

We can see that three design variables affect reliable coverage through different physical mechanisms. The operating frequency f influences both the antenna characteristics and the dispersive propagation term $\mathcal{L}_{\mathrm{ug}}(f)$. In contrast, the antenna radius b and turn number N_{t} do not directly enter $\mathcal{L}_{\mathrm{ug}}(f)$; their effects are mainly introduced through the conductor loss R_{loss}, radiation resistance $R_{\mathrm{rad,soil}}$, and loop inductance L_{c}, which jointly determine the radiation efficiency and available antenna bandwidth. This structural separation suggests that the antenna-geometry variables can first be treated independently of the more strongly coupled frequency dependence.

Furthermore, N_t is restricted to positive integers, whereas b and f are continuous variables. We therefore decompose the original mixed-variable problem into a finite set of turn-number branches by setting

$$N_{\mathrm{t}} = n, \quad n \in \mathcal{N} \triangleq \{N_{\min}, \ldots, N_{\max}\} \tag{16}$$

For a prescribed n, when the operating frequency f is fixed, the propagation term $\mathcal{L}_{\mathrm{ug}}(f)$ in Eq.12 is independent of the antenna radius b. The dependence on b is therefore confined to the antenna radiation and bandwidth characteristics, allowing the optimal radius $b_n^{opt}(f)$ to be characterized from their structural relationships. Once b is eliminated in this manner, the original three-variable mixed optimization problem is reduced to a finite collection of one-dimensional frequency-design branches.

For the radiation efficiency of the underground loop, it is related to the radiation resistance $R_{\mathrm{rad,soil}}$ and the conductor loss R_{loss}. The conductor loss developed can be rearranged as $R_{\mathrm{loss}} = N_{\mathrm{t}} b \Gamma_{\mathrm{o}}(f)$, where $\Gamma_{\mathrm{o}}(f) = \frac{1+\kappa_p}{a}\sqrt{\frac{\pi f \mu_0}{\sigma_c}}$ and $\kappa_p = \frac{R_p}{R_0}$. Furthermore, the radiation resistance established in Section II can be rewritten as $R_{\mathrm{rad,soil}} = N_{\mathrm{t}}^2 b^4 \Gamma_{\mathrm{r}}(f)$, where $\Gamma_{\mathrm{r}}(f) = \mathrm{Re}\left[\tilde{\eta}_{\mathrm{soil}} \frac{2\pi}{3}\left(\frac{\tilde{k}_{\mathrm{soil}}\pi}{\lambda_{\mathrm{soil}}}\right)^2\right]$. Therefore, for the n-th turn-number loop antenna, the radiation efficiency can be expressed as:

$$\eta_n(b, f) = \frac{n\Gamma_{\mathrm{r}}(f) b^3}{\Gamma_{\mathrm{o}}(f) + n\Gamma_{\mathrm{r}}(f) b^3} \tag{17}$$

Its derivative with respect to the antenna radius is:

$$\frac{\partial \eta_n}{\partial b} = \frac{3n\Gamma_{\mathrm{o}}(f)\Gamma_{\mathrm{r}}(f) b^2}{\left[\Gamma_{\mathrm{o}}(f) + n\Gamma_{\mathrm{r}}(f) b^3\right]^2} > 0 \tag{18}$$

For fixed n and f, it means that $\frac{\partial d_{\mathrm{ag,max}}^2}{\partial b} > 0$. It further shows that for any prescribed n and f, increasing the antenna radius improves the reliable coverage within the adopted model. The coverage-optimal radius is therefore the largest radius that simultaneously satisfies the physical and bandwidth constraints.

First, the mechanical-size constraint and the electrically small-loop condition impose an upper bound on the antenna radius for a given operating frequency f,

$$b_{\mathrm{cap}}(f) = \min\left\{b_{\max}, \frac{\xi_{\mathrm{sl}}}{\beta(f)}\right\} \tag{19}$$

where $b_{\max}$ denotes the maximum physically allowable antenna radius, whereas $\xi_{\mathrm{sl}}/\beta(f)$ specifies the largest radius permitted by the electrically small-loop condition. Frequencies for which $b_{\mathrm{cap}}(f) < b_{\min}$ are directly excluded from the feasible set. For the remaining frequencies, the antenna radius is further constrained by the bandwidth required by the communication waveform.

The intrinsic antenna bandwidth for a fixed turn-number branch $N_{\mathrm{t}} = n$ can be expressed as:

$$B_{\mathrm{ant},n}(b, f) = \frac{\Gamma_{\mathrm{r}}(f)b^3 + \Gamma_{\mathrm{o}}(f)/n}{2\pi\mu_0\psi(b)} \tag{20}$$

where $\psi(b) = \ln(8b/a) - 2$. We can see that the effect of the antenna radius on bandwidth is not simply monotonic. Increasing b strengthens the effective damping through the radiation-resistance term $\Gamma_{\mathrm{r}}(f)b^3$, while the logarithmic factor $\psi(b)$, originating from the loop inductance, also varies with the antenna radius. The feasible radius range therefore needs to be characterized explicitly under the minimum bandwidth requirement $B_{\min}$.

To this end, we define the bandwidth-feasibility function

$$g_n(b, f) = \Gamma_{\mathrm{r}}(f)b^3 + \frac{\Gamma_{\mathrm{o}}(f)}{n} - 2\pi\mu_0 B_{\min}\psi(b) \tag{21}$$

The bandwidth requirement $B_{\mathrm{ant},n}(b, f) \geq B_{\min}$ is then equivalently written as $g_n(b, f) \geq 0$. For $g_n(b, f)$, its first and second derivatives are:

$$\begin{aligned} \frac{\partial g_n}{\partial b} &= 3\Gamma_{\mathrm{r}}(f)b^2 - \frac{2\pi\mu_0 B_{\min}}{b} \\ \frac{\partial^2 g_n}{\partial b^2} &= 6\Gamma_{\mathrm{r}}(f)b + \frac{2\pi\mu_0 B_{\min}}{b^2} > 0 \end{aligned} \tag{22}$$

Therefore, for $b > 0$, $g_n(b, f)$ is strictly convex with respect to the antenna radius, indicating a well-defined boundary structure for bandwidth feasibility. Meanwhile, for a prescribed (n, f), the reliable coverage increases monotonically with b. The radius optimization therefore reduces to identifying the largest bandwidth-feasible value within the physically admissible interval $[b_{\min}, b_{\mathrm{cap}}(f)]$. If the physical upper bound $b_{\mathrm{cap}}(f)$ itself satisfies the bandwidth requirement, it directly gives the coverage-optimal radius. Otherwise, provided that the admissible interval still contains bandwidth-feasible radii, the optimal radius must lie on the active bandwidth boundary $g_n(b, f) = 0$.

Furthermore, the active bandwidth boundary $g_n(b, f) = 0$ admits a closed-form expression in terms of the Lambert-W function. Defining

$$\zeta_n(f) = -\frac{3\Gamma_{\mathrm{r}}(f)a^3}{512K_B}\exp\left[6 + \frac{3\Gamma_{\mathrm{o}}(f)}{2n\pi\mu_0 B_{\min}}\right] \tag{23}$$

The two possible real bandwidth-boundary roots are

$$b_{n,k}(f) = \left[-\frac{K_B}{3\Gamma_{\mathrm{r}}(f)}W_k[\zeta_n(f)]\right]^{1/3}, \quad k \in \{0, -1\} \tag{24}$$

where $W_k(\cdot)$ denotes the k-th branch of the Lambert-W function, defined by $W(z)e^{W(z)} = z$. For $\zeta_n(f) \in [-e^{-1}, 0)$, the branches W_0 and W_{-1} correspond to the

two real boundary roots. In the considered case, where increasing b drives the configuration from the bandwidth-feasible region into the infeasible region, the limiting radius is the smaller root and is therefore associated with the principal branch W_0. Thus,

$$b_{n,\mathrm{bw}}(f) = \left[-\frac{2\pi\mu_0 B_{\min}}{3\Gamma_{\mathrm{r}}(f)} W_0[\zeta_n(f)]\right]^{1/3} \tag{25}$$

The optimal radius for each prescribed (n, f) can consequently be expressed as:

$$b_n^{opt}(f) = \begin{cases} b_{\mathrm{cap}}(f), & g_n[b_{\mathrm{cap}}(f), f] \geq 0, \\ \left[-\frac{2\pi\mu_0 B_{\min}}{3\Gamma_{\mathrm{r}}(f)} W_0[\zeta_n(f)]\right]^{1/3}, & g_n[b_{\mathrm{cap}}(f), f] < 0 \text{ and } g_n(b_{\min}, f) \geq 0, \\ \emptyset, & g_n[b_{\mathrm{cap}}(f), f] < 0 \text{ and } g_n(b_{\min}, f) < 0. \end{cases} \tag{26}$$

Substituting the analytically obtained optimal radius $b_n^{opt}(f)$ into (21), the reliable-coverage function associated with the n-th turn-number loop antenna is defined as:

$$\mathcal{F}_n(f) = \frac{P_{\mathrm{t}}\chi_0^2 c^2}{16\pi^2 \gamma_{\mathrm{req}} k_{\mathrm{B}} T_0 F B_{\mathrm{n}}} \frac{\eta_n[b_n^\star(f), f]}{f^2 \mathcal{L}_{\mathrm{ug}}(f)} \tag{27}$$

Since the continuous radius variable b has already been determined by Eq.26, the original mixed optimization problem over (b, N_{t}, f) can be reduced to

$$\max_{b, N_{\mathrm{t}}, f} d_{\mathrm{ag,max}}^2 = \max_{n \in \mathcal{N}_{\mathrm{fea}}} \max_{f \in \mathcal{F}_n} \mathcal{F}_n(f) \tag{28}$$

where $\mathcal{N}_{\mathrm{fea}} \subseteq \mathcal{N}$ denotes the set of integer turn-number branches with nonempty feasible frequency intervals.

Because the operating frequency affects both the antenna radiation characteristics and the dispersive underground propagation in the complete MTER model, $\mathcal{F}_n(f)$ does not admit an explicit closed-form maximizer with respect to f. Within any smooth feasible interval over which the active radius boundary remains unchanged, an interior preferred operating frequency satisfies the following stationarity condition:

$$(1-\eta_n)\left[\frac{\Gamma_{\mathrm{r}}'(f)}{\Gamma_{\mathrm{r}}(f)} - \frac{1}{2f} + 3\frac{b_n^{opt\prime}(f)}{b_n^{opt}(f)}\right] = \frac{2}{f} + \frac{\mathcal{L}_{\mathrm{ug}}'(f)}{\mathcal{L}_{\mathrm{ug}}(f)} \tag{29}$$

Because $b_n^\star(f)$ can be determined by different active physical constraints, its response to the operating frequency depends on the currently active radius boundary. Based on this, $b_n^{opt\prime}(f)/b_n^{opt}(f)$ in Eq.29 can be expressed compactly as:

$$\frac{b_n^{\star\prime}(f)}{b_n^\star(f)} = \begin{cases} 0, & b_n^\star(f) = b_{\max}, \\ -\frac{\beta'(f)}{\beta(f)}, & b_n^\star(f) = \frac{\xi_{\mathrm{sl}}}{\beta(f)}, \\ -\frac{\Gamma_{\mathrm{r}}'(f)[b_n^\star(f)]^3 + \Gamma_{\mathrm{o}}'(f)/n}{3\Gamma_{\mathrm{r}}(f)[b_n^\star(f)]^3 - K_B}, & g_n[b_n^\star(f), f] = 0. \end{cases} \tag{30}$$

Eq.29 characterizes the interior stationary condition for the preferred operating frequency of the n-th turn-number branch. Because $\mathcal{J}_n(f)$ is piecewise defined by different active constraints, the optimal operating frequency of the n-th loop antenna can be determined as:

$$f_n^{opt} = \arg\max \mathcal{F}_n(f), \quad b_n^{opt} = b_n^{opt}(f_n^{opt}) \tag{31}$$

The optimal turn number is then obtained by comparing the maximum reliable coverage achieved by all feasible cases, which is shown as:

$$n^{opt} = \underset{n \in \mathcal{N}_{\text{fea}}}{\arg\max} \mathcal{F}_n(f_n^{opt}) \tag{32}$$

Results

Numerical Results

This section presents numerical results that characterise how the transmitter configuration and underground environment jointly determine reliable UG2AG coverage in the MTER system. We first examine the coverage landscape under a representative

Table 1 Default parameters for numerical evaluation.

Parameter	Value
Operating-frequency range, f	0.5–5 MHz
Loop-radius range, b	0.1–0.5 m
Turn-number range, N_{t}	10–50
Wire radius, a	1 mm
Copper conductivity, σ_{c}	5.8×10^7 S/m
Proximity-effect factor, $\kappa_p = R_p/R_0$	0.5
Maximum transmit power, $P_{\max}$	20 dBm
Signal bandwidth, B_{sig}	10 kHz
Minimum antenna bandwidth, $B_{\min}$	10 kHz
Receiver noise bandwidth, B_{n}	10 kHz
Receiver noise figure, F	6 dB
Reference temperature, T_0	290 K
Target packet delivery ratio, ρ_0	0.9
Required received SNR, γ_{req}	10 dB
Electrically small-loop threshold, ξ_{sl}	0.3
Soil permeability, μ_s	$4\pi \times 10^7$ H/m
Slow-varying power gain, χ_0^2	0.25
Default burial depth, d_{soil}	10 m
Burial-depth range, d_{soil}	4–20 m
Default soil type	silt loam
Default volumetric water content, VWC	28.1%

underground condition to identify the preferred operating region over frequency and turn number. We then extend the analysis to different burial depths, soil textures, and moisture conditions, optimizing the transmitter configuration for each environment. These results provide a systematic assessment of the reliable coverage capability of the MTER system under diverse underground conditions.

Parameter Setup

Unless otherwise specified, the numerical parameters are given in Table 1. The transmitter configuration is optimized over $f \in [0.5, 5]$ MHz, $b \in [0.05, 0.5]$ m, and $N_{\mathrm{t}} \in [10, 50]$. Silt loam with a volumetric water content (VWC) of 28.1% [32] and a burial depth of 3 m is adopted as the reference underground condition. To investigate the influence of underground environments, the burial depth is varied from 2 to 10 m, and four representative soils, namely sand, silt loam, clay loam, and sandy clay loam, are considered using the measured dielectric-relaxation parameters under different moisture conditions illustrated in [32]. The frequency-dependent soil electromagnetic properties are calculated using the dielectric-relaxation model.

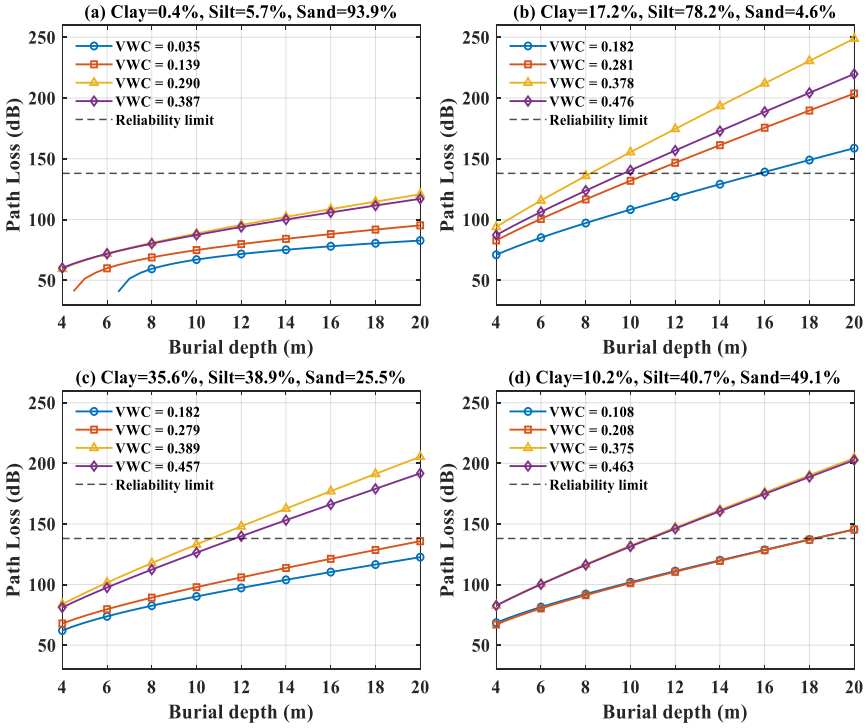


Fig. 2 Path loss of the MTER-enabled UG2AG link at different burial depths and soil moisture conditions.

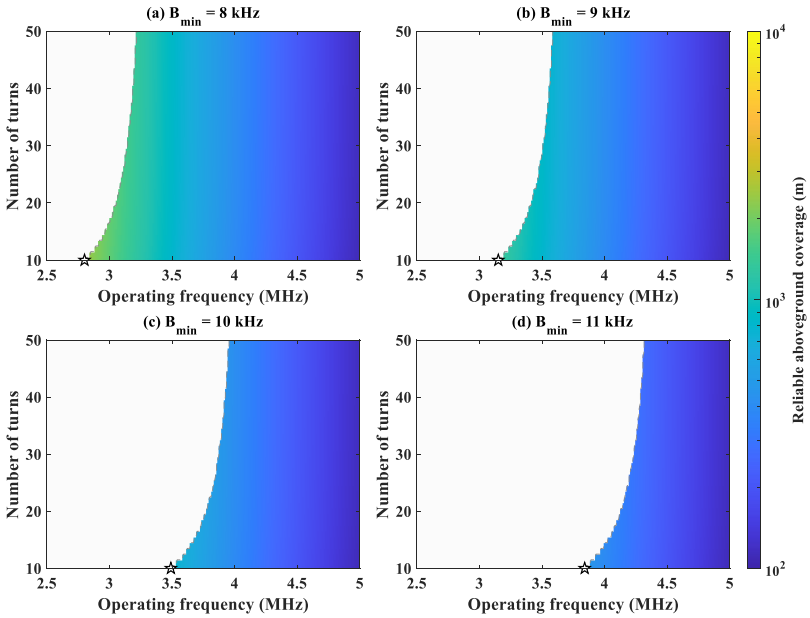


Fig. 3 Reliable aboveground coverage under different minimum antenna-bandwidth requirements.

Path loss Analysis of MTER system for UG2AG communications

Fig. 2 illustrates the path-loss characteristics of the MTER system for UG2AG communications under different soil types and VWCs. A fixed transmitter configuration is adopted, with 10 antenna turns, a coil radius of 20 cm, and an operating frequency of 3 MHz, while the required aboveground transmission distance is set to 800 m. As the burial depth increases, the path loss increases accordingly, with noticeable differences among different underground environments. Nevertheless, the MTER system still exhibits considerable reliable-link potential. For example, under the relatively harsh condition of VWC = 0.378 in Fig. 2(b), reliable 800-m aboveground transmission can still be supported at a burial depth of approximately 8 m. In sandy soil, the path loss remains below the reliability limit throughout the investigated depth range, indicating that reliable communication can be maintained even at a burial depth of 20 m. Overall, these results show that MTER can maintain substantial reliable-link capability over large underground depths and aboveground distances even with a fixed transmitter configuration.

Numerical validation of the transmitter configuration optimization

The reliable aboveground coverage range after optimized transmission configurations under different minimum antenna-bandwidth requirements $B_{\min}$ is shown in Fig. 3. The white regions represent bandwidth-infeasible transmitter configurations, whereas the colored regions indicate the achievable reliable aboveground coverage. As $B_{\min}$ increases from 8 to 11 kHz, the feasible region progressively shifts toward higher operating frequencies, indicating that a more stringent bandwidth requirement eliminates

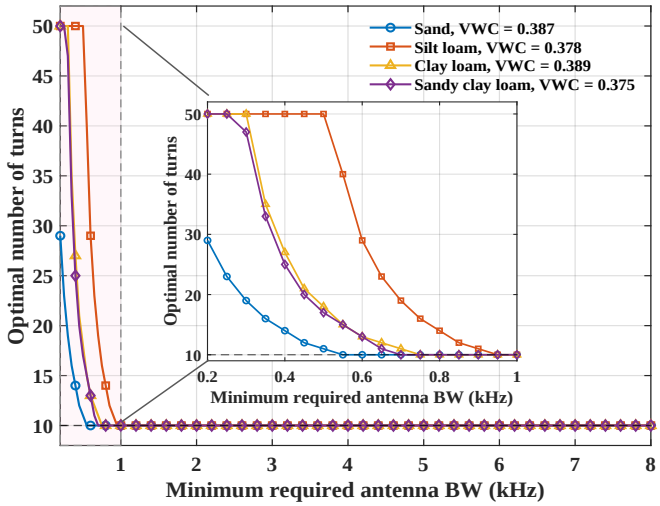


Fig. 4 Dependence of the optimal number of loop turns on the minimum required antenna bandwidth.

an increasing portion of the low-frequency configurations. Meanwhile, the optimal operating frequency also increases with $B_{\min}$, while the optimal turn number remains at its lower bound of the turn number range N_t. This behavior reflects the tradeoff between antenna-bandwidth feasibility and underground propagation loss, where lower frequencies are generally favorable for underground propagation, and a larger $B_{\min}$ requires operation at higher frequencies to maintain sufficient antenna bandwidth. Consequently, the optimum tends to occur close to the boundary of the bandwidth-feasible region, where the required bandwidth can be satisfied without incurring an excessive propagation penalty.

Reliable coverage under different underground conditions

To further explain why the optimal number of turns always approaches its minimum value under bandwidth requirements, Fig. 4 shows the relationship between coil turns and minimum antenna bandwidth requirements in four underground environments. Under a relaxed bandwidth requirement, a larger number of turns can be preferred. However, as $B_{\min}$ increases, N_t rapidly decreases and eventually converges to $N_t = 10$ in all considered environments. Under the adopted coil model, increasing the turn number can improve the radiation efficiency, but it simultaneously narrows the intrinsic antenna bandwidth and contracts the feasible configuration region. The resulting bandwidth and propagation penalties eventually outweigh the marginal efficiency gain, driving the optimum toward the minimum turn number.

Fig. 5 compares the optimized transmitter configurations under different soil types and moisture states at a burial depth of 10 m. The optimal coil radius and operating frequency exhibit dependence on the underground environment, whereas the optimal number of turns remains at $N_t = 10$ for all feasible cases. In particular, the optimal

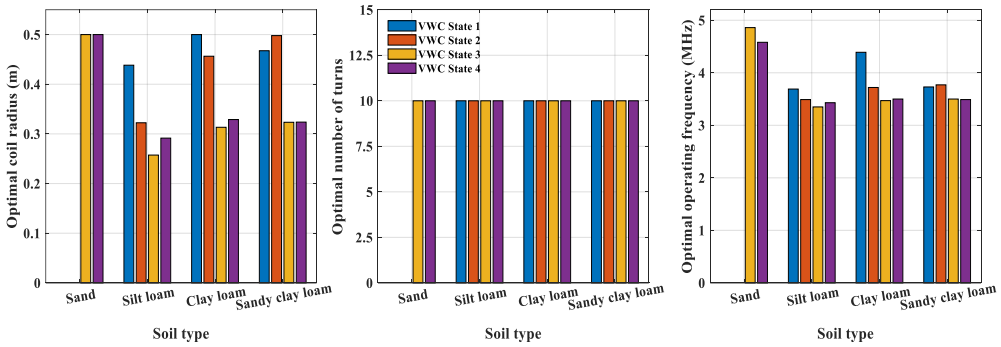


Fig. 5 Environment-dependent optimal transmitter configurations for MTER-enabled UG2AG communication.

coil radius varies approximately from 0.25 to 0.5 m, while the optimal operating frequency ranges from about 3.3 to 5 MHz. These variations indicate that soil-dependent electromagnetic properties substantially affect the preferred antenna size and operating frequency. By contrast, the persistent solution $N_t = 10$ is consistent with the bandwidth-driven behavior discussed above. More narrowly, under the adopted coil model, increasing the turn number can improve radiation efficiency, but it simultaneously narrows the intrinsic antenna bandwidth and contracts the feasible configuration region. The associated bandwidth and propagation penalties therefore outweigh the marginal efficiency gain at the nominal bandwidth requirement, driving the optimum toward the minimum turn number. In addition, the missing bars for some sandy-soil states indicate that no feasible configuration satisfying the adopted constraints is obtained at the considered burial depth.

Fig. 6 further shows how the reliable aboveground coverage varies with burial depth. In all environments, the reliable coverage decreases rapidly as the underground depth increases, owing to the increasing attenuation within the lossy soil medium. Nevertheless, substantial differences are observed among soil types and moisture states. Sandy soil provides the most favorable propagation conditions, maintaining kilometer-scale or larger aboveground coverage even at relatively large burial depths. In contrast, several higher-loss states of silt loam, clay loam, and sandy clay loam experience a much faster reduction in the reliable aboveground coverage, with the achievable coverage eventually falling to the meter scale as the burial depth increases. The results also show that the effect of moisture is not strictly monotonic, because each measured VWC state corresponds to a different set of soil electromagnetic parameters. Overall, these results demonstrate that the achievable UG2AG coverage is strongly environment-dependent and that adapting the transmitter configuration to the underground conditions is important for exploiting the reliable-link potential of the MTER architecture.

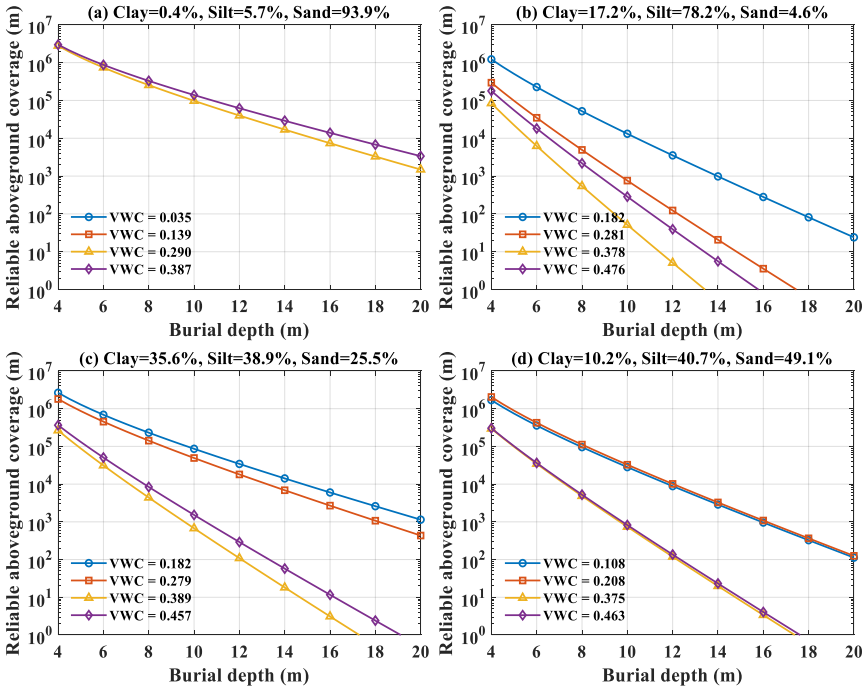


Fig. 6 Maximum reliable aboveground coverage at different burial depths and underground environments.

Field Results

The above analysis characterizes the reliable coverage of the MTER link and reveals how the transmitter configuration, operating frequency, and bandwidth requirement jointly shape its communication capability. Based on these link-level results, we further implemented a practical MTER prototype to examine whether the low-frequency, bandwidth-constrained link can support end-to-end data delivery in a realistic underground environment. In this experiment, the transmitter employs a loop antenna with a radius of 20 cm and 12 turns, while the communication system operates at approximately 2 MHz. Furthermore, the set bandwidth is 10 kHz, and a QPSK waveform has an occupied bandwidth of about 8.44 kHz.

To emulate the propagation conditions of deeply buried UG2AG links, a massive mine pillar with a characteristic dimension of about 10 m is used to construct a large-scale through-rock propagation scenario. The transmitter and receiver are deployed on different sides of the pillar, such that the direct Tx–Rx path is strongly obstructed by the intervening rock mass. As illustrated in Fig. 7, the deployment further involved approximately 11 m and 40 m of propagation on the two sides of the pillar, with an angular separation of approximately 50°. In this experimental scenario, the transmitter and receiver are separated by approximately 35 m, including about 15 m of propagation through the rock mass and an additional 20 m of propagation through air. In this scenario, an image is employed as the payload to assess the complete transmission

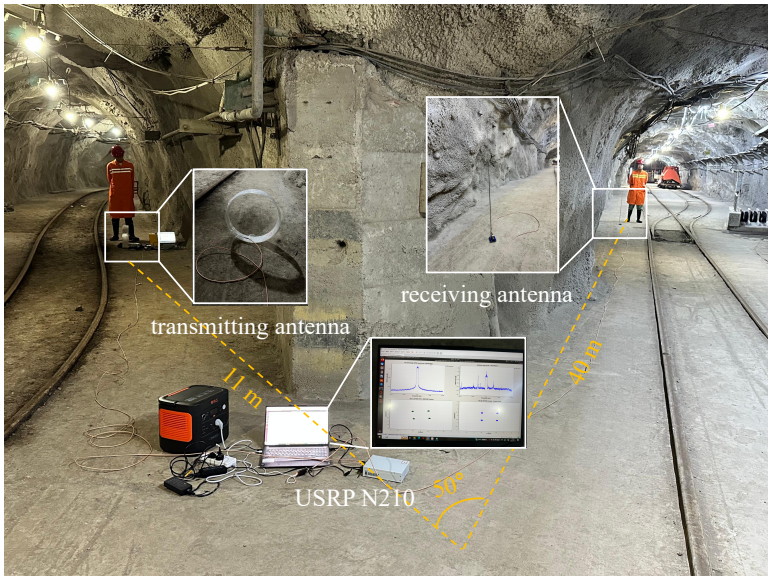
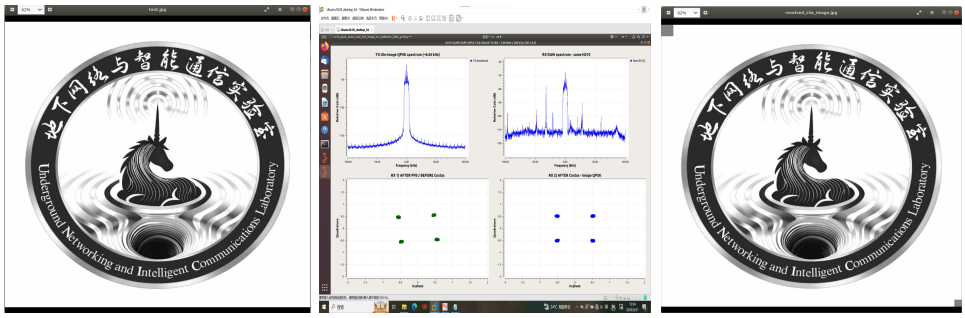


Fig. 7 Field experimental setup of the MTER communication system in an underground mine.

process, including waveform transmission, signal acquisition, synchronisation, QPSK demodulation, and data reconstruction.

Fig. 8 presents the end-to-end image-transmission results obtained in the underground mine. Fig. 8(a) shows the original test image used as the transmitted payload. The corresponding physical-layer signal characteristics are shown in Fig. 8(b). After propagation through the obstructed mine environment, the desired signal remains clearly observable in the received spectrum. Four identifiable QPSK symbol clusters are obtained before carrier recovery, indicating successful carrier recovery and symbol demodulation. Based on the recovered data, the image is successfully reconstructed at the receiver, as shown in Fig. 8(c). During this transmission, PDR is 99.608%, and the detected-packet BER is about 2.213×10^{-5}. The experimental result demonstrates successful end-to-end payload delivery over the practical MTER link.



(a) (b) (c)

Fig. 8 Field experimental results of end-to-end image transmission over the MTER link.

Discussion

This study demonstrates that the reliable aboveground coverage in MTER-enabled UG2AG communication is determined by characteristics of the transmitter, underground propagation, and bandwidth constraints. Therefore, the appropriate transmitter configuration varies with the underground environment, and stricter bandwidth requirements can significantly change the feasible working area and reduce the achievable coverage range. The field experiment further demonstrates end-to-end QPSK image transmission over a strongly obstructed underground link, showing that MTER communication can support practical information delivery under realistic mine conditions. Future work will focus on broader field validation under different underground environments and on further improving the robustness and adaptability of practical MTER communication systems.

Data availability

No datasets are associated with this study.

Code availability

The simulation code used to generate the results of this study is available from the corresponding author upon reasonable request.

Acknowledgements

This work was supported in part by the National Key Research and Development Program of China under Grant 2024YFB2908802, in part by the National Natural Science Foundation of China under Grant 62371200, Hubei Key Research and Development Program under Grant 2025BCB120, and Natural Science Foundation of Wuhan under Grant 2025040601020215, and HUST Basic Research Support Program under Grant 2026BRB011.

Author Contributions

G.Z. and G.L. conceived the study and designed the research. G.Z., Y.L., and X.G. conducted the mine experiment. G.Z. wrote the manuscript and organized the figures and tables. G.L. supervised the overall project execution and revised the manuscript. All authors reviewed the manuscript.

References

[1] Lin, K., Alouini, M.-S.: Toward sustainable subterranean mmtc: Space-air-ground-underground networks powered by lorawan and wireless energy transfer. IEEE Wirel. Commun. (2025)

[2] Zhang, H., Liu, G., Xu, Y., Jiang, T.: Loraaid: Underground joint communication and localization system based on lora technology. IEEE Trans. Wirel. Commun. **23**(5), 5248–5260 (2023)

[3] Di Renzone, G., Parrino, S., Peruzzi, G., Pozzebon, A., Bertoni, D.: Lorawan underground to aboveground data transmission performances for different soil compositions. IEEE Trans. Instrum. Meas. **70**, 1–13 (2021)

[4] Vuran, M.C., Salam, A., Wong, R., Irmak, S.: Internet of underground things in precision agriculture: Architecture and technology aspects. Ad Hoc Netw. **81**, 160–173 (2018)

[5] Moiroux-Arvis, L., Cariou, C., Chanet, J.-P.: Evaluation of lora technology in 433-mhz and 868-mhz for underground to aboveground data transmission. Comput. Electron. Agric. **194**, 106770 (2022)

[6] Lin, K., Hao, T.: Experimental link quality analysis for lora-based wireless underground sensor networks. IEEE Internet Things J. **8**(8), 6565–6577 (2020)

[7] Sambo, D.W., Forster, A., Yenke, B.O., Sarr, I., Gueye, B., Dayang, P.: Wireless underground sensor networks path loss model for precision agriculture (wusn-plm). IEEE Sens. J. **20**(10), 5298–5313 (2020)

[8] Zhao, G., Lin, K., Hao, T.: A feasibility study of lorawan-based wireless underground sensor networks for underground monitoring. Comput. Netw. **232**, 109851 (2023)

[9] Cotrim, R., Assis, F., Santos Brito, A., Peixouto, Y.S., Peixouto, L.S.: Multi-hop lora-based underground network for monitoring soil moisture in agriculture. Comput. Electron. Agric. **227**, 109592 (2024)

[10] Sørensen, T.B., Maurya, P., Christensen, P.H., Damsgaard, S.B., Duus, S., Moradi, F.: Experimental investigation and path loss modeling for 868mhz ism band communication between pipe monitoring sensors and above ground receivers. IEEE Internet Things J. (2025)

[11] Zhang, H., Liu, G., Jiang, T.: Parameter configuration scheme for optimal energy efficiency in lora-based wireless underground sensor networks. IEEE Trans. Veh. Technol. **74**(6), 9961–9966 (2025)

[12] Zhao, G., Lin, K., Chapman, D., Metje, N., Hao, T.: Optimizing energy efficiency of lorawan-based wireless underground sensor networks: A multi-agent reinforcement learning approach. Internet Things **22**, 100776 (2023)

[13] Lin, K., Hao, T., Yu, Z., Zheng, W., He, W.: A preliminary study of ug2ag link quality in lora-based wireless underground sensor networks. In: 2019 IEEE 44th Conference on Local Computer Networks (LCN), pp. 51–59 (2019). IEEE

[14] Liu, G., Zhang, H., Deng, S., Jiang, T.: Conductor-aware wireless underground sensor networks based on magnetic induction: Research challenges. IEEE Netw. **38**(6), 259–266 (2024)

[15] Tan, X., Sun, Z., Akyildiz, I.F.: Wireless underground sensor networks: Mi-based communication systems for underground applications. IEEE Antennas Propag. Mag. **57**(4), 74–87 (2015)

[16] Liu, G.: Data collection in mi-assisted wireless powered underground sensor networks: Directions, recent advances, and challenges. IEEE Commun. Mag. **59**(4), 132–138 (2021)

[17] Sun, Z., Akyildiz, I.F.: Magnetic induction communications for wireless underground sensor networks. IEEE Trans. Antennas Propag. **58**(7), 2426–2435 (2010)

[18] Kisseleff, S., Akyildiz, I.F., Gerstacker, W.H.: Survey on advances in magnetic induction-based wireless underground sensor networks. IEEE Internet Things J. **5**(6), 4843–4856 (2018)

[19] Guo, H., Sun, Z., Sun, J., Litchinitser, N.M.: m^2i: Channel modeling for metamaterial-enhanced magnetic induction communications. IEEE Trans. Antennas Propag. **63**(11), 5072–5087 (2015)

[20] Zhao, G., Liu, G., Li, Q., Hu, Y.: Magnetic-transmitter to electric-receiver system for underground-to-aboveground communication exploiting induction field and radiation field. IEEE Trans. Green Commun. Netw. (2026)

[21] Souapiebe, E.-P., Sambo, D.W., Mbala, R.M., Dayang, P., Meddahi, A., Förster, A., Saynbe, M.R.: Node placement approaches for wireless underground sensor network deployment. Ad Hoc Netw., 104411 (2026)

[22] Yin, X., Wang, K., Liu, J., Zhang, X., Yao, H., Wang, H., Luan, H., Tan, K.: Link quality characterization and deployment optimization of wireless underground sensor networks for precision agriculture. IEEE Sens. J. (2025)

[23] Guo, H., Sun, Z.: Increasing the capacity of magnetic induction communication using mimo coil-array. In: 2016 IEEE Global Communications Conference (GLOBECOM), pp. 1–6 (2016). IEEE

[24] Guo, H., Ofori, A.A.: Joint channel and antenna modeling for magnetic induction communication in inhomogeneous media. IEEE Open J. Commun. Soc. **1**, 1457–1469 (2020)

[25] Guo, H., Sun, Z., Wang, P.: Multiple frequency band channel modeling and analysis for magnetic induction communication in practical underwater environments. IEEE Trans. Veh. Technol. **66**(8), 6619–6632 (2017)

[26] Liu, Y., Kim, H.-H., Kim, H.: Loop-type ground radiation antenna for dual-band wlan applications. IEEE Trans. Antennas Propag. **61**(9), 4819–4823 (2013)

[27] Boswell, A., Tyler, A.J., White, A.: Performance of a small loop antenna in the 3-10 mhz band. IEEE Trans. Antennas Propag. **47**(2), 51–56 (2005)

[28] Li, Q., Liu, G., Zhao, G.: Boundary demarcation of magnetic induction communication. IEEE Trans. Antennas Propag. (2026)

[29] Wheeler, H.: Small antennas. IEEE Trans. Antennas Propag. **23**(4), 462–469 (1975)

[30] Balanis, C.A.: Antenna Theory: Analysis and Design. John wiley & sons, ??? (2015)

[31] Sun, Z., Akyildiz, I.F., Hancke, G.P.: Dynamic connectivity in wireless underground sensor networks. IEEE Trans. Wirel. Commun. **10**(12), 4334–4344 (2011)

[32] Bobrov, P.P., Kroshka, E.S., Muzalevskiy, K.V.: The effect of dielectric relaxation processes on the complex dielectric permittivity of soils at frequencies from 10 khz to 8 ghz—part ii: Broadband analysis. IEEE Trans. Geosci. Remote Sensing **62**, 1–11 (2023)

Figure legends

Figure 1. Architecture of the MTER-enabled underground-to-aboveground communication system. A magnetic loop antenna is deployed underground as the transmitter, while an electric-antenna gateway is located aboveground. The underground portion of the link exploits the induction-dominated field before the radiating component develops and propagates across the soil–air interface toward the gateway. The geometric parameters indicate the underground and aboveground propagation distances, antenna burial depth, gateway height, and refraction geometry. MTER denotes magnetic-transmitter-to-electric-receiver, and UG2AG denotes underground-to-aboveground.

Figure 2. Path loss of the MTER-enabled UG2AG link at different burial depths and soil moisture conditions. The four panels show the path loss for soils with different clay, silt, and sand contents: **a)**, sand-dominated soil; **b)**, silt loam; **c)**, clay loam; and **d)**, sandy clay loam. Each curve represents a different volumetric water content. The horizontal dashed line indicates the reliability-related path-loss threshold. VWC denotes volumetric water content.

Figure 3. Reliable aboveground coverage under different minimum antenna-bandwidth requirements. The heat maps show the achievable reliable aboveground coverage as a function of operating frequency and number of loop turns for minimum required antenna bandwidths of **a)**, 8 kHz; **b)**, 9 kHz; **c)**, 10 kHz; and **d)**,

11 kHz. The coloured regions indicate feasible transmitter configurations, with colour representing the reliable aboveground coverage distance, whereas the white regions correspond to infeasible configurations. The star in each panel marks the configuration that provides the maximum reliable coverage.

Figure 4. Dependence of the optimal number of loop turns on the minimum required antenna bandwidth. The curves show the optimal number of turns under representative soil and moisture conditions as the minimum antenna-bandwidth requirement increases. The inset enlarges the low-bandwidth region, where the optimal number of turns changes rapidly with the bandwidth requirement. The results illustrate the tradeoff between transmitter radiation performance and antenna bandwidth.

Figure 5. Environment-dependent optimal transmitter configurations for MTER-enabled UG2AG communication. The three panels show the optimized **a)**, loop radius; **b)**, number of turns; and **c)**, operating frequency for different soil types and volumetric water-content states. The grouped bars correspond to the four moisture states considered for each soil type. The results show that the preferred transmitter configuration varies with the underground electromagnetic environment.

Figure 6. Maximum reliable aboveground coverage at different burial depths and underground environments. The four panels show the reliable aboveground coverage for soils with different clay, silt, and sand contents: **a)**, sand-dominated soil; **b)**, silt loam; **c)**, clay loam; and **d)**, sandy clay loam. Each curve corresponds to a different volumetric water content. The vertical axis is shown on a logarithmic scale. VWC denotes volumetric water content.

Figure 7. Field experimental setup of the MTER communication system in an underground mine. The magnetic loop transmitting antenna and electric receiving antenna are deployed in different tunnel sections with a large rock and concrete obstruction between them, forming a strongly obstructed propagation link. The enlarged insets show the transmitting and receiving antennas, while the USRP N210 platform is used for signal generation, transmission, reception, and processing. The dashed lines indicate the approximate geometry of the experimental link.

Figure 8. Field experimental results of end-to-end image transmission over the MTER link. a), Original test image used as the transmitted payload. **b)**, Measured physical-layer signal characteristics during transmission and reception, including the transmitted and received spectra and the QPSK constellations before and after carrier recovery. **c)**, Image reconstructed from the received data. The recovered QPSK constellations and the close visual agreement between the transmitted and reconstructed images demonstrate successful end-to-end data transmission. QPSK denotes quadrature phase-shift keying.